



Analysis of Global and Local Hydrodynamic Instabilities on a High-Speed Jet Diffusion Flame via Time-Resolved 3D Measurements

Rongxiao Dong¹ · Qingchun Lei¹ · Yeqing Chi¹ · Erzhuang Song¹ · Wei Fan¹

Received: 29 June 2020 / Accepted: 9 February 2021 / Published online: 27 February 2021
© The Author(s), under exclusive licence to Springer Nature B.V. part of Springer Nature 2021

Abstract

Measurements of 3D flame edge dynamics were made on a high-speed jet diffusion flame to assess the global/local hydrodynamic instability. The flame was generated by issuing high-speed ethylene ($U_j = 170$ m/s) into a low-speed vitiated hot coflow ($U_c = 1.5$ m/s), resulting in a hydrodynamic shear layer instability at the interface between combustion products and ambient flow. The measurements used a high-speed camera combined with nine-headed fiber endoscopes to simultaneously collect both the soot radiation and chemiluminescence projections of the flame from nine views, based on which 3D flame edges were obtained via computed tomography at 15 kHz. The measurements clearly capture the time-varying, 3D instantaneous flame edge structures with fine-scale corrugations, enabling the observation of small-scale vortices' evolution. The flame edge deformations induced by those vortices were calculated globally and locally to infer the relationship between global and local flame edge oscillations. Results show that various local oscillation frequencies exist at different locations along the flow direction for such a highly sheared flame. They are dominated by the periodical formation and motion of various localized, small-scale vortices. The local oscillations are much severer than the global oscillation, indicating a self-suppression of the instabilities between these local oscillations. The suppression mechanism is attributed to the constructive and destructive interference behavior of the local disturbances. The global oscillation of the flame edge turns out to be the linear superposition of local oscillations at different locations.

Keywords 3D measurements · Flame edge dynamics · Global and local hydrodynamic instabilities · Non-premixed · Computed tomography

✉ Qingchun Lei
lqc@nwpu.edu.cn

¹ School of Power and Energy, Northwestern Polytechnical University, 127 West Youyi Road, Xi'an 710072, Shaanxi, People's Republic of China

1 Introduction

Combustion instabilities remain a critical issue that limits the development of a wide operating range, low-emission combustion systems. One of the essential mechanisms that induce and sustain unstable combustion is the coupling of acoustic instability with self-excited hydrodynamic instability. Hydrodynamic instability is associated with various factors, including the buoyancy, shear layer, density and fraction gradients, etc., which poses a challenging field of research.

Experimental measurements to characterize the hydrodynamic instability are desired. Of particular interests are the measurements of flame edge dynamics since the time-varying flame edge behaviors are strongly related to the flame-vortex interaction and thus can provide insights regarding the phenomenology of the hydrodynamic instability of the flame (Lee and Santavicca 2003; Kolhe and Agrawal 2007; Schlimpert et al. 2016). The major challenges of the experimental investigations are thus attributed to the time-varying nature of these flows. Past efforts for the measurements of flame edge dynamics have been primarily based on the 2D techniques, such as the luminescence/chemiluminescence of self-emissions of combustion products (Shin et al. 2011; Allison et al. 2017), planar Mie-scattering of seeded tracer particles (Alabdeli et al. 2006; Shanbhogue et al. 2009a; Long and Hargrave 2011), Schlieren imaging (Kolhe and Agrawal 2007) and planar laser-induced fluorescence (PLIF) (Steinberg et al. 2010; Allison et al. 2015; Doleiden et al. 2019). In these techniques, the 2D flame edge contours are first extracted based on the measured signal distributions, and their motions are then tracked shot-to-shot to infer the flame fluctuation behaviors.

However, the major disadvantage of these techniques is that they only provide incomplete information on the flame edge motion. For example, the line-of-sight nature of the luminescence/chemiluminescence technique prevents it from resolving localized phenomena or spatially resolved flame edge structure. Planar Mie scattering and PLIF can overcome the line-of-sight limitation, but they cannot provide the flame oscillation information out of the measurement plane. This disadvantage becomes severer for the conditions where various local flame oscillations exist in the flame at different locations. For instance, Kolhe and Agrawal (2007) found that in a jet diffusion flame, the instabilities developed in the shear layer between the flame edge and outer vortices vary along the axial direction resulting in different local dominant frequencies. Subsequent numerical studies (Nichols and Schmid 2008; Qadri et al. 2015) further identified multiple types of instability modes that originated from different locations of the flame that govern the global instability dynamics. This requires time-resolved 3D measurements further to quantify the relationship between the local and global instabilities and provide validation data to numerical results.

Fortunately, extending the capability of the above-mentioned 2D techniques to 3D measurements becomes possible with the recent advancement in lasers, cameras, and computing techniques. The strategies include laser sheet scanning (Cho et al. 2014; Weinkauff et al. 2015) and the computed tomography (CT). Notably, recently, a significant amount of work has demonstrated the potential of the CT strategy combined with luminescence/chemiluminescence (Floyd et al. 2011; Worth and Dawson 2012; Moeck et al. 2013; Li and Ma 2015; Huang et al. 2019), Mie scattering (Upton et al. 2011; Lei et al. 2014), Schlieren (Ishino et al. 2015; Nicolas et al. 2015), and LIF (Ma et al. 2017; Li et al. 2017; Halls et al. 2017; Pareja et al. 2019) to measure the 3D flame surface properties with sufficient temporal resolution (i.e., up to 20 kHz Ma et al. 2016).

However, to date, most demonstrations of CT flame measurements are dedicated to improving the CT technique itself. The post-processing and analysis of the retrieved time-series of 3D flame data to understand combustion phenomena are rare. Wiseman et al. (2017) have developed a series of post-processing algorithms for measuring flame surface area, flame curvature, flame thickness, and the normal component based on the reconstructed 3D data of a weakly turbulent premixed flame. In this work, we aim to show how the measured time-varying 3D data can be utilized to obtain useful information such as flame edge deformations to study local/global hydrodynamic instability on a high-speed jet diffusion flame. Another aim is to identify how the local oscillations at different locations affect the global oscillation of the flame and to complement the theory of flame transfer functions (FTF) or flame describing functions (FDF) (Candel et al. 2014; Gatti et al. 2019; Gaudron et al. 2019).

With the above understandings, this work reports an application of CT technique combined with luminescence to resolve the 3D flame edge dynamics of a high-speed jet diffusion flame at 15 kHz, based on which the relationship of the local and global hydrodynamic instabilities is identified. The measurements were obtained using a single camera with a nine-headed fiber bundle, an approach recently developed to significantly facilitate the implementation of the CT technique (Anikin et al. 2010). This work aims to address two crucial aspects in the tomographic measurements of turbulent flames: (a) the validity and capability using a single camera combined with fiber endoscopes to resolve the 3D structures and dynamics of high-speed, highly turbulent flames beyond tens of kilohertz; (b) using the 3D data (i.e., tracking the 3D flame edge) to interpret the hydrodynamic instabilities in such highly sheared flames.

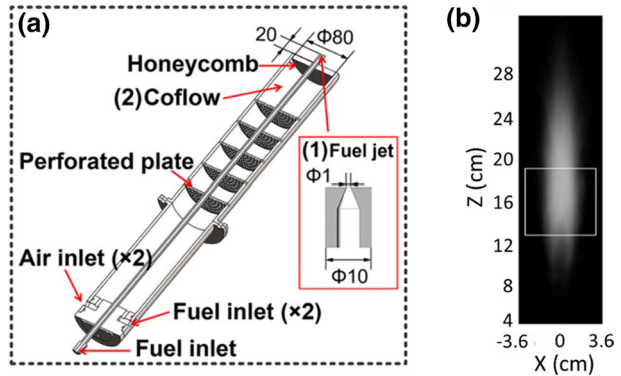
In the rest of this paper, Sect. 2 describes the experimental setup, including details of the burner used in this work, testing conditions, and the hardware used in the 3D diagnostics. Section 3 describes the 3D tomographic reconstruction methods and validation results. Section 4 discusses the 3D measurement of the flame edge dynamics and the analysis of the local and global hydrodynamic instabilities. Section 5 then summarizes and concludes the paper.

2 Experimental Setup

2.1 Burner and Operating Conditions

Figure 1a shows the schematic of the burner tested in this study. The burner was designed to generate a high-speed, highly sheared jet diffusion flame. The specifics of this burner have been described in our previous work (Liu et al. 2019a), and only a summary is provided here. The burner consisted of a primary central tube (1 mm ID), from which issued pure C_2H_4 . The central tube was surrounded by an 80 mm ID hot coflow. The hot coflow was generated by a lean premixed C_2H_4 /air flame stabilized on an annular stainless-steel honeycomb. The equivalence ratio of the coflow was 0.48, and the velocity of the coflow was 1.5 m/s. The tip of the central nozzle was 20 mm above the honeycomb. To generate the turbulent flames, pure C_2H_4 was continuously issued from the central tube at 1.2 atm into the hot coflow, resulting in a jet exit velocity of $U = 170$ m/s and jet Reynolds number of $Re = 22,516$. At this specific operating condition, the overall flame length was ~ 27 cm, as shown in the time-averaged flame luminescence image in Fig. 1b. The white box in Fig. 1b centered at $Z = 16$ cm represents the field-of-view in the subsequent CT 3D measurements.

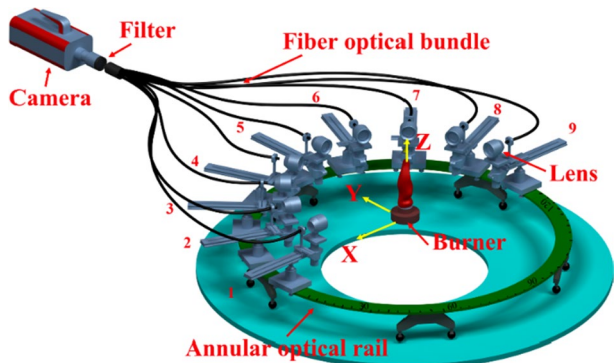
Fig. 1 Burner and turbulent flame tested in this study: **a** schematic of the burner and **b** time-averaged luminescence image of the flame at the operating condition



2.2 3D Measurement System

Figure 2 shows the schematic of the experimental system to obtain instantaneous 3D flame measurements. As mentioned in the operating condition of the burner, the target flames were highly turbulent and high-speed. Therefore, the projection measurements from various orientations were captured simultaneously and instantaneously. As shown in Fig. 2, a customized fiber bundle and one CMOS camera (iX-speed 720) were applied to accomplish such projection measurements. More specifically, the customized fiber bundle consisted of nine inputs, which were then assembled into one output. Each input was an assembly of 90,000 single-mode fibers in an array of 300×300 , so the output end transmitted a total of 810,000 ($9 \times 90,000$) image elements. The fiber endoscopes and the camera were aligned so that one image element transmitted by one fiber approximately corresponded to one pixel on the camera. In the experiments, each fiber endoscope input was equipped with an AF Nikon lens (50 mm f/1.4D). The nine fiber bundles were installed on an annular rail so that they were all at the same co-plane and with the same objective distance to the target flame. The signal from all fiber endoscopes at the output end was then recorded on the same CMOS array of the camera. The camera was equipped with another AF Nikon lens (50 mm f/1.4D) and a broadband filter (i.e., 400–700 nm). The cameras were operated at a frame rate of 15 kHz and an exposure time of $66.12 \mu\text{s}$.

Fig. 2 Schematic of the experimental setup to obtain instantaneous 3D flame measurements



To better illustrate the geometry parameters of the setup, the following Cartesian coordinate system was established as follows. The origin was defined at the center of the burner, the X-axis was defined along the optical axis of fiber endoscope 1, the Y-axis was defined to be perpendicular to the X-axis, and the Z-axis was defined to be along the direction of the flow. Based on this definition, the angles formed between the optical axis of each fiber endoscope and the positive X-axis were 0° , 16.6° , 35.0° , 52.4° , 74.6° , 93.0° , 110.4° , 124.2° , 142.0° , respectively, determined by an improved camera calibration method (Xia et al. 2019). The objective distance of all fiber endoscopes to the center of the burner was 39.3 cm. These measured projections were then used as the inputs to an inversion algorithm as described in Sect. 3 to reconstruct the 3D luminescence field of the target flame.

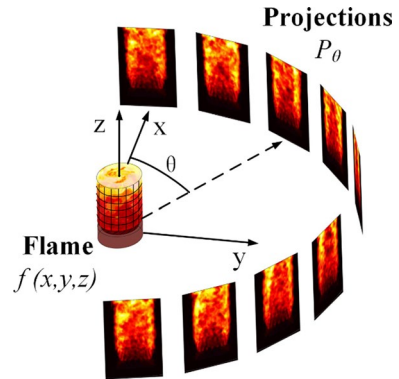
It is worth noting that with the above-mentioned measurement scheme and the diffusion nature of the ethylene flame, the signal measured contains both the thermal radiation of soot and the chemiluminescence in the visible range. However, as the goal of this work is to investigate the hydrodynamic shear layer instability, the flame edge dynamics extracted based on the luminescence signals (soot thermal radiation) can also represent the vortex-induced hydrodynamic instability of the flame for the following reasons. First, even though there are deviations in the position of chemical radicals (i.e., OH/OH*) and soot particles, their motion/fluctuation behaviors should be similar since they both fluctuate as a response to the local vortex (i.e., the vortex formation, rolling and propagation). The time scales for both soot formation and chemical reaction are significantly faster compared to the vortex propagation time scales. It is demonstrated in Katta et al. (2009) that in an ethylene jet diffusion flame, the magnitude of flame oscillations decreases with the amount of soot generated in the flame; however, the frequency of the oscillations does not change. The same oscillation frequency of soot particles and other combustion radicals indicates that they respond to the same vortex of the turbulent flow field. The suppression of the oscillation magnitude by the increased soot concentration is, however, due to the cooling effects of thermal radiation. In the present work, with the injecting velocity of 170 m/s, the Froude number is calculated to be larger than 10. When the Froude number is larger than 5, the jet flame oscillation is suggested to be dominated by the momentum (Delichatsios 1993). Thus, a stronger response of the combustion products (whether they are intermediate radicals or soot particles) is expected to the local vortex. Second, we have performed a test experiment to examine the oscillation behaviors of the soot particles and the OH* radicals. In the experiment, two high-speed cameras (equipped with appropriate filters) were used to measure the simultaneous soot radiation signals and OH* chemiluminescence, respectively. Results show that although the soot radiation signals and OH* chemiluminescence are with deviation in the position, the oscillating frequencies of flame edge obtained based on two signals at different downstream locations are almost identical. We cannot perform the 3D OH* chemiluminescence measurement since the current fiber endoscopes do not transmit the ultraviolet signals.

3 3D Tomographic Reconstruction and Validation

3.1 Mathematic Formulation

Figure 3 shows the mathematical formulation of a typical 3D tomographic problem of turbulent flames. In the problem, the 3D distribution of the sought flame property is discretized into voxels, denoted as $f(x, y, z)$. An imaging lens collects the 2D line-of-sight

Fig. 3 Mathematical formulation of a reacting flow tomography problem



integrated emission signals of the flame from different orientations. Those 2D images are named as projections and denoted as $P_\theta(s)$. The measured $P_\theta(s)$ depends on the viewing angle θ , which represents the orientation of f with respect to the acquisition plane; s denotes the projection coordinate. In experimental measurement setups that the dimension of the flame is much smaller than the objective distance, the measured $P_\theta(s)$ corresponds to parallel lines perpendicular to the Z-axis. Thus, $P_\theta(s)$ is known as the Radon transform of $f(x, y, z)$ and can be formulated as:

$$P_\theta(s) = R\{f(x, y, z)\} = \int_{\psi(\theta, s)} f(x, y, z) dl \quad (1)$$

where R denotes the Radon transform, and $\psi(\theta, s)$ is a parameter representing the line sight with a given viewing angle θ and the distance of the line to the origin. The imaging model used to compute the sensitivity matrix in this work is the parallel beam imaging model. Generally, the use of parallel beam projection theory is an approximation since the camera collects light in a fan-shaped manner. When the object distance relative to the object diameter is large, the rays can be assumed to be parallel (Floyd et al. 2009). In the present case, the object distance (39.3 cm) is sufficiently larger than the object diameter (6.4 cm). Thus, it can be assumed that the error resulted from the parallel beam assumption is negligible.

The goal of the above tomography problem is to solve $f(x, y, z)$ with measured $P_\theta(s)$. Suppose the projections are sufficient (i.e., hundreds) and are sampled continuously around the flame, as in the medical tomography problem. In that case, the $f(x, y, z)$ may be reconstructed analytically using the Fourier slice theorem, which states that the Fourier transform of $P_\theta(s)$ with respect to s at a constant z_0 equals to the 2D Fourier transform of $f(x, y, z_0)$ along s with constant viewing angle θ (Kak et al. 2002). Unfortunately, in turbulent flame tomography, it is impractical to obtain many such projections. In turbulent flame tomography, the projections are sampled discretely from a few viewing orientations, and the f can be reconstructed using an algebraic iteration technique in this case. An algebraic algorithm, named the multiplicative algebraic reconstruction technique (MART), is used to perform the tomography reconstruction in the current work. Mohri et al. (2017) have conducted a thorough study to evaluate a similar algebraic iterative algorithm (e.g., ART) on the tomographic reconstruction of highly turbulent swirl flames. They concluded that in the most sparsely sampled cases, e.g., when N_q (# of views)=3 and $N_q=4$, decreasing the total number of unknowns, or voxels, actually aids the system to generate better

results. They thus predicted that even a small number of views (e.g., 4) appears to be sufficient to observe larger asymmetries in the flame, such as those caused by coherent vortex cores or maybe even thermoacoustic fluctuations with a suitably reduced number of voxels. In the present work, the ratio of the total number of voxels (e.g., $150 \times 150 \times 150$) to the total number of pixels (e.g., $9 \times 300 \times 300$) is ~ 4 , which is in a safe range for 9 views to yield a good reconstruction according to Mohri et al. (2017). The domain dimensions are $6.4 \times 6.4 \times 6.4 \text{ cm}^3$ with a grid spacing of $\sim 0.43 \text{ mm}$. The termination criterion, as described in Mishra et al. (2004), is employed in this work to control the termination of convergence in MART algorithm.

3.2 Validation of the Method

This work presents two kinds of validation for the tomography algorithm to reconstruct the 3D structure of the highly turbulent flame. The first validation involves a numerical phantom test. The second validation involves the reconstruction of 3D flame using partial experimental measured projections, the reproduction of projection which is not used in the foregoing reconstruction, and the comparison between the reproduced and measured projections. This section describes the first validation. The second validation will be illustrated with the experimental results in Sect. 4.1.

In the phantom test, the 3D OH radical distribution of the same jet diffusion flame computed by the large eddy simulation (LES) of our previous work (Liu et al. 2019a) was used as the phantom. Projections of this phantom were calculated according to Eq. (1) with the same nine viewing orientations as in the experimental setup of Fig. 2. The chain branching reaction $\text{H} + \text{O}_2 \rightarrow \text{OH} + \text{O}$ is used for the LES-calculations of OH. Though the OH distribution used in the phantom study does not match with the reconstructed field in the experiments (i.e., soot radiation), it is assumed they exhibit the flame structure at the same turbulence level. And the purpose of the LES phantom study is to assess and validate the capability of the CT technique to resolve the flame structure at a similar turbulence level to the experiment.

A total of 0.6° of the view registration (VR) error, a major source of noise for combustion tomography (Liu et al. 2019b), was randomly added to the projections. The reconstruction is shown and compared with the phantom in the second row of Fig. 4. In the second set of validation, both 0.6° of view registration (VR) error and 2% of Gaussian noise (estimated according to the signal-to-noise ratio) were artificially added to the projections to further quantify the effect of the VR error and imaging noise on the reconstruction. The reconstruction and comparison are shown in the third row of Fig. 4. In Fig. 4, the comparison from three sets of horizontal slices of the original phantom and reconstructions is shown. The comparison at those horizontal planes allows a critical assessment of the reconstruction quality, as suggested in Mohri et al. (2017). To quantify the reconstruction quality, the overall reconstruction error (e) and correlation coefficient (r) were calculated as:

$$e = \frac{\sum_{n=1}^N |f_n^{rec} - f_n|}{\sum_{n=1}^N f_n} \text{ and } r = \frac{\text{cov}(ff^{rec})}{\sigma_f \sigma_{f^{rec}}} \quad (2)$$

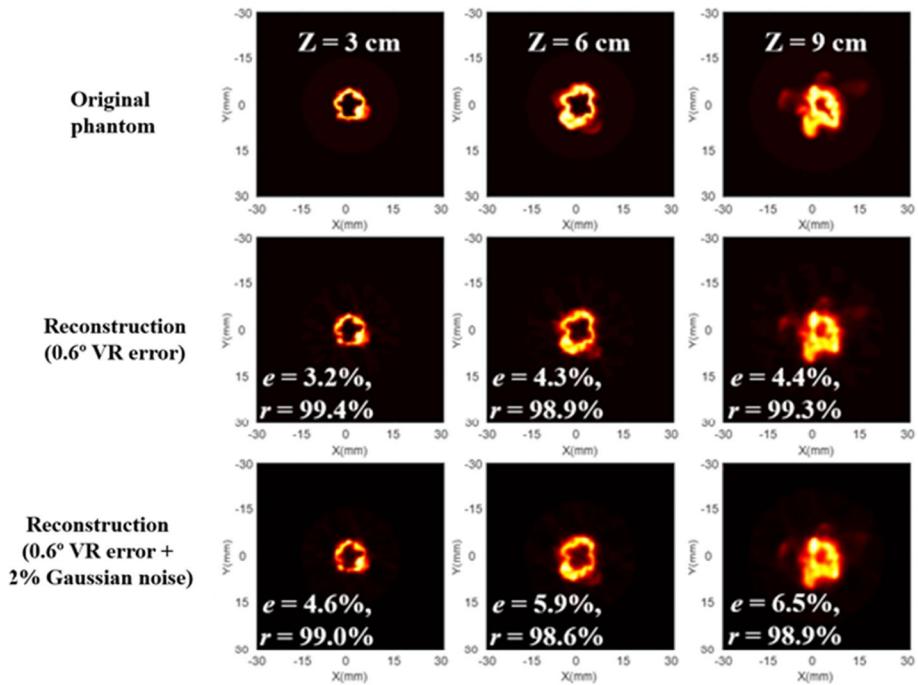


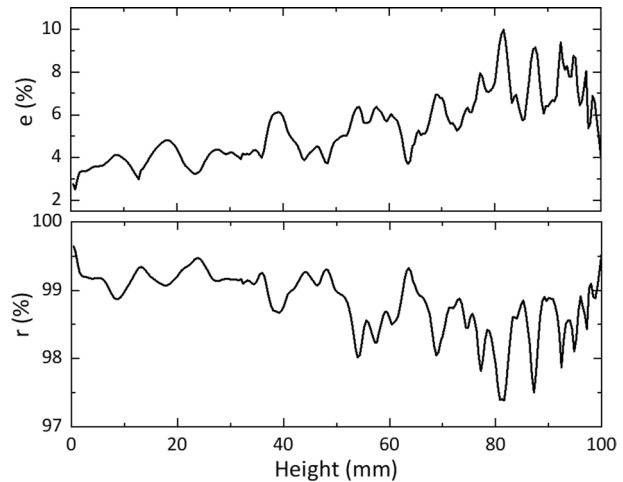
Fig. 4 Comparison of the phantom and reconstruction at three sets of horizontal slices

where n is the voxel index, N the total number of voxels; f represents the known phantom, f^{rec} the reconstruction; cov and σ represent the convolution and standard derivation, respectively. Good agreement can be observed between the original and reconstructed flame structures with both VR error and imaging noise considered. In addition, the reconstruction error resulting from Gaussian noise is below half of that resulted from view registration uncertainty, indicating that the angle calibration uncertainty brings primary reconstruction error. The Gaussian noise induces little degradation in the correlation coefficient.

Figure 5 further shows the overall reconstruction error and correlation coefficient along the axial direction with both the VR error and image noises considered. As shown, the reconstruction fidelity obviously decreases (e increases and r decreases) with height above the burner, indicating larger deviations from the perfect reconstruction. This is due to the increased corrugation and wrinkling of the downstream flame structure. The overall reconstruction accuracy is within acceptance (with e below 10% and r larger than 97%). Note that, in the phantom validation, the flame extends all the way to the last voxel row on the top of the computational domain. Thus, a dip in error observed at the largest height is due to the stochastic nature of turbulent flows. The error of the reconstruction in the black background region is below 1% by calculating the error for vertical slices. Results in Figs. 4 and 5 demonstrate the capability and robustness of the CT system in the present work to resolve both the large-scale structures and details of the target flame with acceptable accuracy when noisy projections are involved.

Based on the pure tomography algorithm validation, the sensitivity of the discretization scheme on the flame edge deformation is also evaluated. More specifically, a

Fig. 5 The overall reconstruction error and correlation coefficient along the downstream distance of the flame



high-resolution LES phantom (with a dimension of 256^3 determined by the maximum usage of 128G RAM of the workstation) is used to generate the nine projections with the same orientations in the experiments. Those projections are used to reconstruct three sets of flame distribution: high-resolution reconstruction (with the same dimension to phantom), low-resolution reconstruction (with the dimension of 150^3), and low-resolution reconstruction (i.e., 150^3) with noise (including both VR error and image noise). The flame edge deformation between two consecutive time instances is calculated and compared for phantom and reconstructions. Comparison shows good agreement (i.e., $e = 1.74\%$ for high-resolution reconstruction, $e = 5.19\%$ for low-resolution reconstruction, and $e = 5.65\%$ for low-resolution reconstruction with noises).

Further validation of the CT technique is illustrated in Sect. 4 by comparing the particular features of the flame between the reconstruction and the raw projection measurement.

4 Experimental Results and Discussion

4.1 Tomographic Reconstructions

After the description and numerical validation of the tomography reconstruction, this section shows the experimental demonstration and validation of tomographic reconstruction on the jet diffusion flame. First, Fig. 6 shows a set of measured raw projection examples containing the soot radiation and visible chemiluminescence captured by all nine fiber endoscopes and the camera. The camera captured nine projections transmitted by fiber endoscope inputs 1 through 9 simultaneously, with the projection transmitted by each fiber endoscope occupying approximately one-ninth of the camera chip (i.e., $\sim 300 \times 300$ pixels). The only pre-processing step performed on these raw images before reconstruction is the signal normalization of nine projections based on the linearity calibration of signal transmission of nine fiber endoscopes. As shown in Fig. 6, the flame is highly turbulent and has a distinctly different structure in each view, illustrating the 3D nature of the flame structure and the necessity to resolve it.

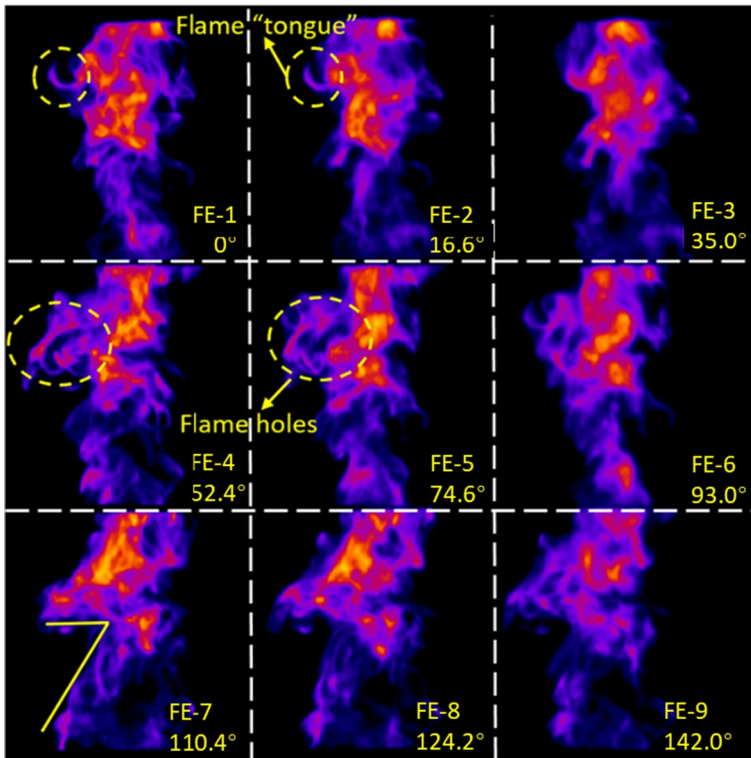


Fig. 6 A sample of instantaneous projection measurement containing the soot radiation and visible chemiluminescence captured by nine-headed fiber endoscopes from nine different perspectives

The projections shown in Fig. 6 were fed into the subsequent tomography reconstruction program using the MART algorithm to retrieve the 3D instantaneous luminescence distribution of the flame. The reconstruction results are shown in Fig. 7 from four different viewing angles. As seen, the reconstruction successfully resolves both the overall flame structure and also the detailed turbulent wrinkles (as highlighted in the ovals). For example, the measured projection on the seventh fiber endoscopes shown in Fig. 6 (F-7) indicates that the flame has an approximate “7” shape when viewed from this particular orientation. The 3D reconstruction shown in Fig. 7c captured the overall “7” shape. Furthermore, the measured projection reveals flame holes and the flame tongue at various locations, as highlighted in the ovals. These holes and the flame tongue are successfully captured by the 3D reconstruction. Besides, several vertical and horizontal slices of reconstruction are shown in Fig. 7e to further exhibit the spatially resolved distribution of the reconstructed field.

Figure 8 shows a more detailed comparison of the specific feature of the flame tongue, as seen in Fig. 6 highlighted with ovals to further validate the 3D reconstruction. This flame tongue can be seen in the 1st and 2nd projections in Fig. 6 of the luminescence from the flame. Figure 8a shows a zoom-in raw image of this feature from the 1st projection. The reconstruction of this feature is shown in Fig. 8b, c from the side and the top view, respectively. It can be seen from Fig. 8b that the thickness of the reconstructed feature in the axial direction (1.29 mm) is a good representation of its thickness in the raw data (0.85 mm).

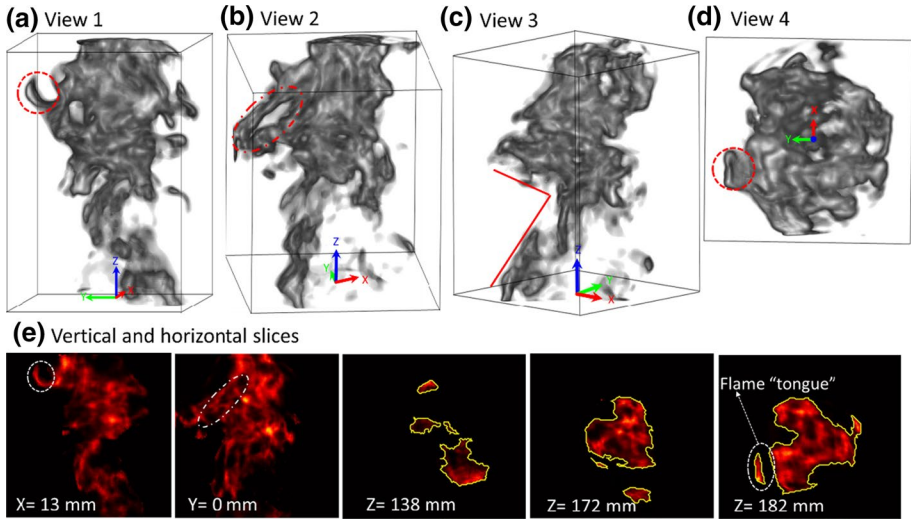
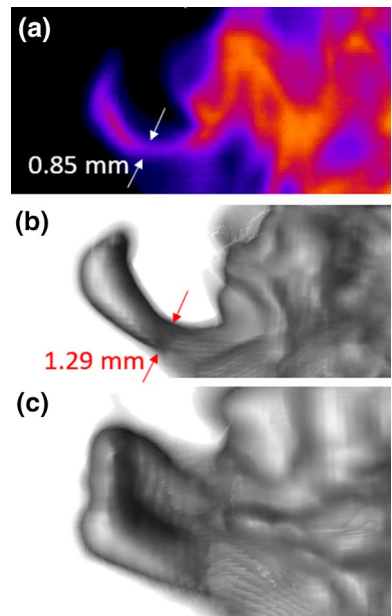


Fig. 7 First row: 3D reconstructions of flame from four different views; second row: several vertical and horizontal slices of the reconstruction

Fig. 8 The flame tongue as seen **a** in the original data from fiber endoscope 1, **b** in the reconstruction viewing along the X axis, and **c** in the reconstruction from the top



Though the spatial resolution of 3D reconstruction cannot compete with the raw 2D data, it provides 3D information in all three directions. For instance, Fig. 8c shows the structure and size of the flame tongue from the top view. However, such information cannot be revealed from the original 2D projection data.

Though comparisons in Figs. 7 and 8 are not sufficient to prove the correctness of the reconstruction, they provide a necessary condition. In order to further quantitatively

Fig. 9 Comparison between the measured projection and the reproduced projection

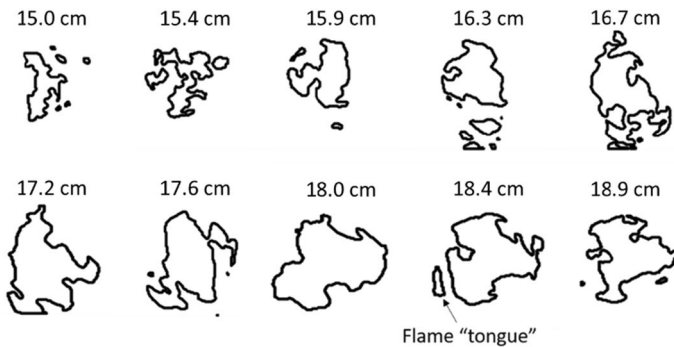
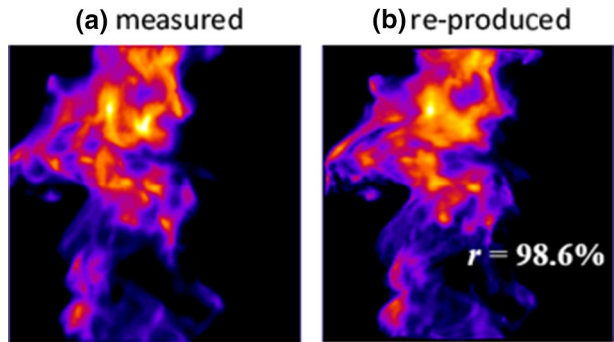


Fig. 10 Flame edge contours in planes perpendicular to the burner centerline. Heights above the burner exit are indicated. The edge contour of the flame tongue is observed at $Z=18.2$ cm

validate the method, the tomographic reconstruction was performed again using the first eight (i.e., F-1 to F-8) projections in Fig. 6. The 9th projection was reproduced based on Eq. (1) and then was compared with the 9th measured projection. The comparison was shown in Fig. 9. Good agreement can be seen from the measured and reproduced projections. The correlation coefficient was calculated to be larger than 98.5%, further validating the high fidelity of the reconstruction technique.

Based on the 3D reconstruction in Fig. 7, Fig. 10 shows the horizontal flame edge contours extracted from the 3D reconstruction shown in Fig. 7. Note that it is usually more difficult to capture such multiple horizontal slices of flame simultaneously at different heights with conventional 2D measurements. In this work, the flame edge contour was determined based on a thresholding method (Ma et al. 2016). In this method, the average background level is determined by comparing the raw projection measurements with/without flames (i.e., 1000 frames for each case). And the background level is calculated to be 0.1% of the maximum luminescence intensity. This background level is then used as the threshold value to the 3D reconstructions to determine the flame edge. Other threshold values, e.g., 0.2% and 0.5%, are tested to extract the flame edges, and similar contours are obtained. It should be noted that after the threshold value is determined, both inner boundaries and outer boundaries can be extracted. The outer boundaries represent the flame edge, and the inner boundaries indicate the holes inside the flame. We exclude the inner boundaries by judging if the boundary is enclosed by another outer boundary, if yes, we call it the

‘child feature’ while the outer boundary is called the ‘parent feature’ accordingly. Only the parent boundaries are extracted in this work. In this way, the flame edge contours shown in Fig. 10 represent the outermost layer of the raw voxels. As discussed previously (see Sect. 2), the tomographic reconstruction procedure produces 150 planes spaced 0.43 mm vertically from 130 to 194 mm above the fuel jet exit. In Fig. 10, only ten of these slices are shown at a vertical spacing of ~ 4.3 mm. Those horizontal flame edge contours show a narrower, more corrugated structure at the lower height and a broader, smoother structure at the higher height. The analysis of fluctuation behaviors of those flame edge contours will be described in the following section (see Sect. 4.3).

4.2 Time-Varying Flame Dynamics

To display the time-series of the 3D reconstructions, two movie files are first provided: the first video shows the evolution of the 3D flame structures in a time period of 6 ms, containing 130 consecutive frames of 3D instantaneous tomography reconstructions (Visualization 1); the second video shows a 360° rotating animation of one 3D reconstructed flame (Visualization 2).

Four sample frames in the time-series movie with a relatively large time interval (Δt) of 1.6 ms are shown in Fig. 11, which reveals several critical physical phenomena of the flame. For example, at $t=0$ ms, an isolated soot pocket rises from the left bottom of the FOV. In the subsequent images at $t=1.6$ ms and 3.2 ms, the pocket increases in volume and merges into the main flame, respectively. Also, note that during the time from 3.2 to 4.8 ms, large-scale flame wrinkling, a result of vortex formation, roll-up, and convection, is clearly observed, indicative of the existence of local vortex-induced instability. The diameter of the formed vortex at $t=4.8$ ms is ~ 7 mm, as shown in Fig. 11d. The downstream movement speed of the vortex is ~ 15 m/s calculated by tracking its centroid in the 15 consecutive reconstructions from 3.2 to 4.8 ms. During this time period, the vortex induces an average air-penetration volume of 4300 mm^3 to the flame (by counting the zero-value voxel number in the flame region). By screening the reconstructed data, a vortex with a similar scale and convective speed as in Fig. 11d occurs periodically almost every 3 ms around this location. This implies the local flame edge disturbance induced by the vortex oscillates at a frequency of ~ 333 Hz. And the mean magnitude of the flame edge deformation due to the vortex stretching at each height is estimated to be 96 mm^2 (i.e., $4300 \text{ mm}^3/15 \text{ m/s}/3 \text{ ms}$). The above analysis shows the usefulness of time-varying 3D flame data to estimate the vortex-induced flame edge oscillations. The next section will further quantify the flame

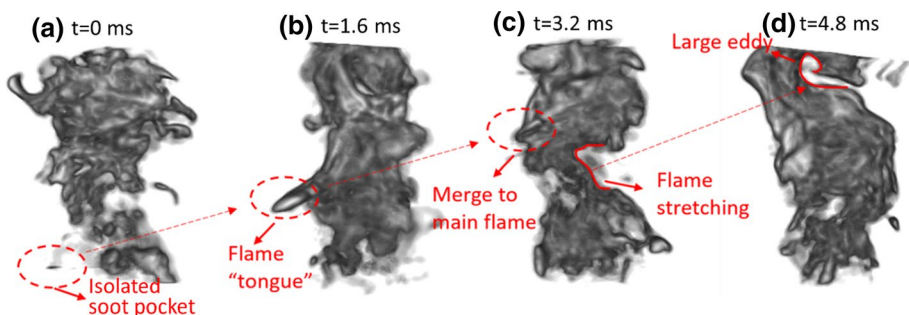


Fig. 11 Evolution of overall 3D flame edge structures at four time instances with $\Delta t = 1.6$ ms

dynamics by calculating the flame sheet density (FSD), the oscillation amplitude (A'), frequency (f), and phase (φ) of both the global and local flame edge deformation.

4.3 Quantification of Flame Dynamics

First, the 3D FSD is calculated based on the flame edge surface area per unit volume (using a sample sized of 400 frames of reconstruction):

$$FSD = \lim_{\Delta x \rightarrow 0} \frac{\bar{A}}{\Delta x^3} \quad (3)$$

where \bar{A} is the time-averaged surface area in the interrogation box. At each point of the three-dimensional flame edge brush \bar{A} is measured by counting the flame edge voxels within an interrogation box of $\Delta x^3 = 1.28 \text{ mm} \times 1.28 \text{ mm} \times 1.28 \text{ mm}$. Distributions of the 3D FSD at several different downstream distances are shown in Fig. 12. As shown, the high value of the FSD distributes in an irregular region close to the central axis at the lower height (i.e., $Z = 134 \text{ mm}$), which indicates a severer fluctuation of the flame edge at this location and a possible global extinction occurring upstream of this height since the FSD distribution appears to be an accumulation of a series of small and unsteady flame edge contours. The global extinction at the lower heights can also be inferred from the time-varying movie (Visualization 1). Note that the observation of global extinction is consistent with the previous LES results where the blow-off appears with high-frequency and high-magnitude fluctuations of the flame surfaces (Zhang and Mastorakos 2015). The flame tends to be relatively stable with the height increase as the FSD s are observed to distribute in a relatively stationary toroidal region (i.e., $Z = 158 \text{ mm}$ to 182 mm), indicating the re-ignition and re-establishment of the flame. Such a stable region of the flame spans $\sim 30 \text{ mm}$, and the flame becomes unstable again by observing the gradual shrink of the inner core of the toroid (i.e., $Z = 190 \text{ mm}$).

The FSD shown in Fig. 12 indicates the significant variance of local flame fluctuations along downstream distances. To further investigate the local flame fluctuation behaviors and how they affect the global fluctuation of the flame. The global and local flame edge deformation are calculated. Figure 13 shows the global and local flame edge deformation at two consecutive time instants and the calculation strategy. For example, the blue and red

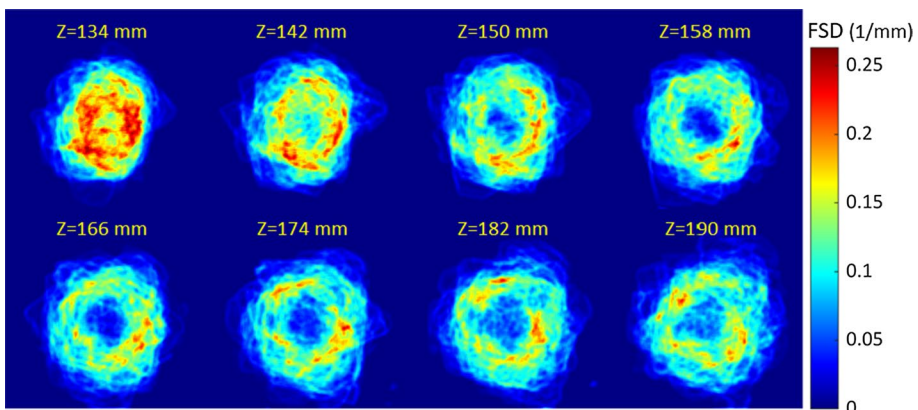


Fig. 12 Flame sheet density at different heights along downstream distances

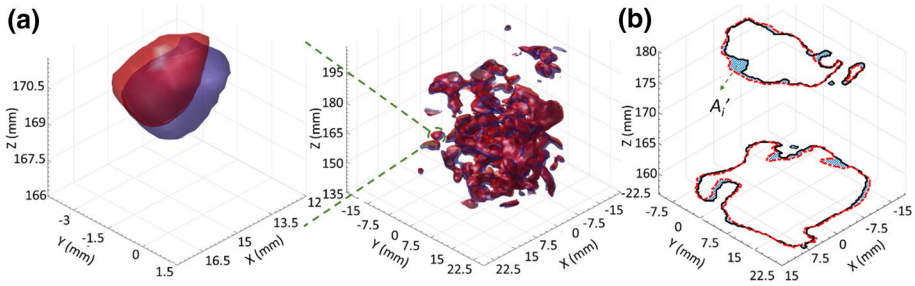


Fig. 13 Global (a) and local (b) flame edge deformation during two consecutive time instants with the time interval of $66.12 \mu\text{s}$; the blue surface (or solid black line) represents the flame edge at the former time instant, the red surface (or red dashed line) at the latter time instant

surfaces shown in Fig. 13a are the global flame edge surfaces extracted at two consecutive time instants. The time interval is $66.12 \mu\text{s}$. A localized small flame pocket of the flame is zoomed-in in Fig. 13a to show the discrepancy of the two flame edge surfaces. As can be seen, the flame edge slightly changes, indicating the time resolution of 15 kHz is sufficient to capture the flame edge change in the present flame. Figure 13b shows two examples of the local flame edge deformations at two different heights, wherein the solid black line represents the flame edge at the former time instant, the red dashed line at the latter time instant. It is clearly observed that the deformation magnitude varies for different parts of the flame contour. Some parts of the contour are compressed by the surrounding flow, some are stretched, and some are almost unchanged. And the flame edge was observed to respond primarily to large-scale fluctuations in the flow at the shear layer. Those observations first demonstrate the utility of the 3D technique to analyze the flame edge deformation. In contrast, 2D techniques only capture the flame deformation from one specific orientation. Second, the results indicate a significant interaction of the local flow turbulence with the flame edge. For the local flame edge deformation, the deformation magnitude (A') is defined and calculated as the summation of the area formed by the two intersected flame edge contours at each height (i.e., $A' = \sum A'_i$, a sample of A'_i is marked as the dashed region in Fig. 13b). Similarly, the global flame deformation magnitude (V') is defined and calculated as the summation of the volume formed by the two intersected flame edge surfaces.

The calculated global flame edge deformation magnitude during a time period of 26 ms (corresponding to 400 frames) is shown in Fig. 14a. In this time period, V' varies in a range of $5000\text{--}8000 \text{ mm}^3$, and the mean flame edge deformation is 6175 mm^3 . The RMS variation of V' is 595 mm^3 , approximately 9.6% of the mean flame edge deformation. Fig. 14b shows the power spectral density (PSD) and the frequency response of the V' in Fig. 14a. The dominant frequency response of the V' occurs at 113 Hz and 301 Hz , respectively.

Similarly, the local flame edge deformation magnitude and PSD at two local heights of the flame in Fig. 13b are shown in Fig. 15. The A' varies by as much as 200 mm^2 at both heights. The mean values of A' are 109 mm^2 and 101 mm^2 , close to the estimated mean value in Fig. 11 (i.e., 96 mm^2). The calculated RMS fluctuations of the A' are 26.9% of the mean flame edge deformation at $Z=134 \text{ mm}$ and 32.8% of the mean flame edge deformation at $Z=190 \text{ mm}$, respectively. These values are notably larger than that observed in the global deformation (9.6%), indicating that the local fluctuations are much severer than the global fluctuation, and it appears to exist a self-suppression of the instabilities between these local oscillations. The largest frequency response of the

Fig. 14 Global flame edge deformation: **a** temporal fluctuations of the deformation over a 26 ms time period and **b** power spectral density and frequency response. The dashed line depicts the mean flame edge deformation of 6175 mm^3 . The RMS fluctuation of the flame edge deformation is 595 mm^3

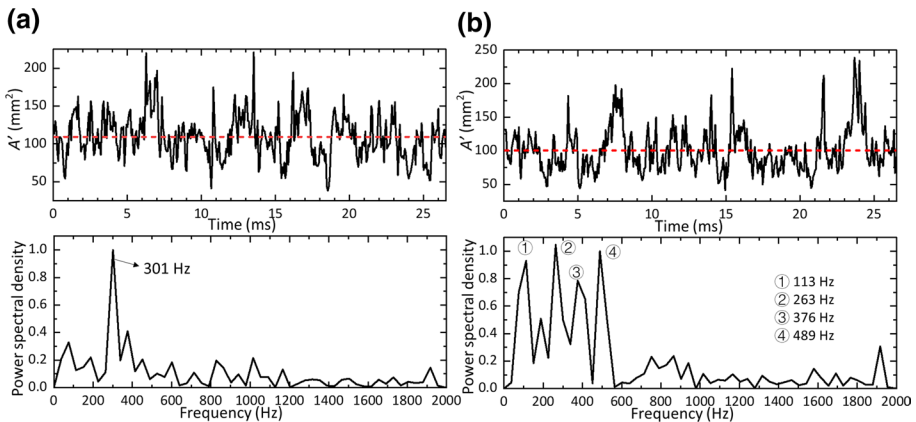
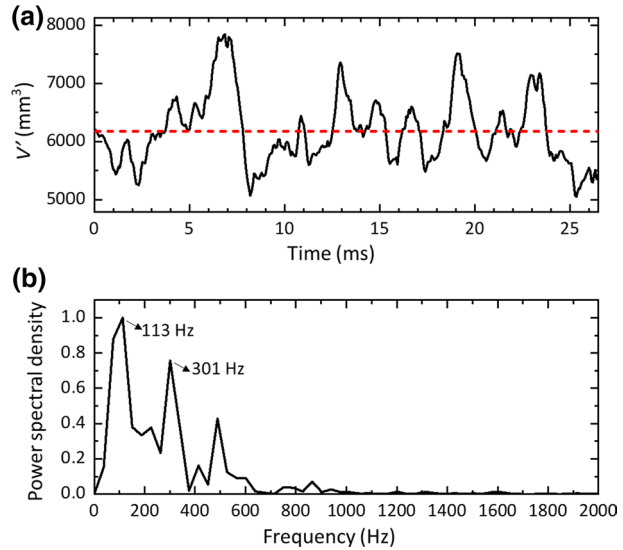
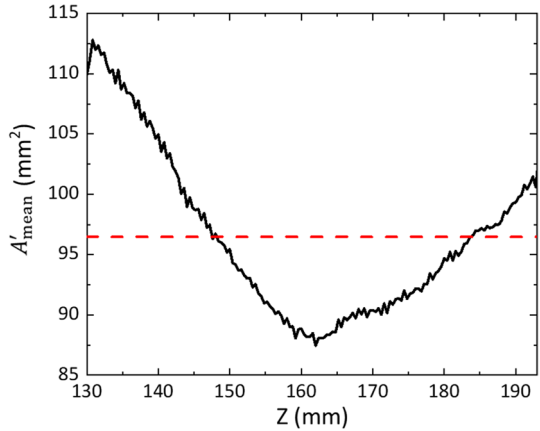


Fig. 15 Local flame edge deformation fluctuation magnitude and power spectrum density of frequency response at two downstream distances: **a** $Z=134 \text{ mm}$ and **b** $Z=190 \text{ mm}$. The red dashed line shows the mean value of A'

flame edge deformation at $Z=134 \text{ mm}$ occurs at 301 Hz, while there are four dominant frequencies (113 Hz, 263 Hz, 376 Hz, and 489 Hz) at $Z=190 \text{ mm}$. Two of them (113 Hz and 301 Hz) are matched with the dominant frequencies in the global flame edge deformation. Another dominant frequency of 376 Hz at $Z=193 \text{ mm}$ is close to the estimated frequency of 333 Hz based on the movement of the local vortex shown in Fig. 11. Those observations imply a complicated coupling of local oscillations to govern the global oscillation.

It is thus needed to evaluate the local flame edge fluctuations along the whole height of the flame in the field of view (FOV). Figure 16 first shows the mean deformation magnitude (A'_{mean}) of the local flame edge oscillations at different downstream locations.

Fig. 16 Mean flame edge deformation along the downstream distances



As shown, the A'_{mean} plot shows two distinct regions: a rapid descending region and a re-ascending region. This observation agrees well with the FSD plots in Fig. 12, in which the flame is undergoing an “unstable, stable, and unstable” cycle. The FSD s in Fig. 12 suggest that the unstable region is caused by the local extinction of the flame, which results in the large magnitude of the flame edge deformation. The A'_{mean} plot also suggests that the stable region maintains in a range of 35 mm (from $Z=148$ mm to 183 mm), in which the A'_{mean} is below the averaged value (dashed line).

Figure 17 shows the largest frequency response of the local flame edge oscillations at different downstream locations (solid black line). Based on the similarity of the frequency responses at different locations, the whole flame height can be divided into six subregions. The circled number above the line in Fig. 17 represents the subregion index, and the star next to the number indicates there exist other high-power–frequency responses in this subregion. In the first subregion ($Z=130$ mm to 146 mm), the single, largest frequency response occurs at 301 Hz (referring to Fig. 15a). In the second subregion ($Z=146$ mm to 153 mm), the largest frequency response occurs at 902 Hz, and other high-power

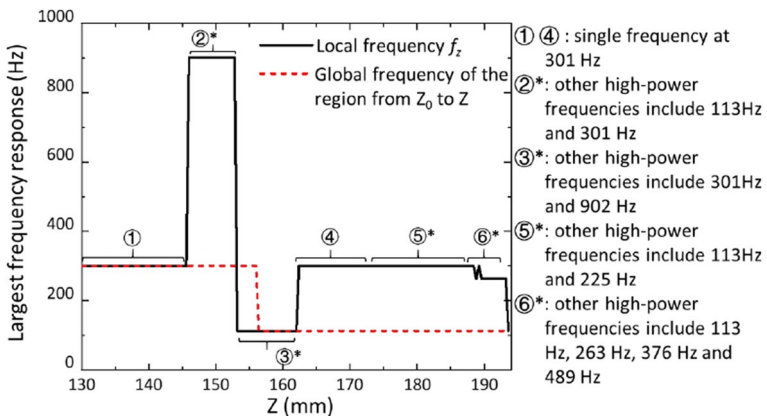


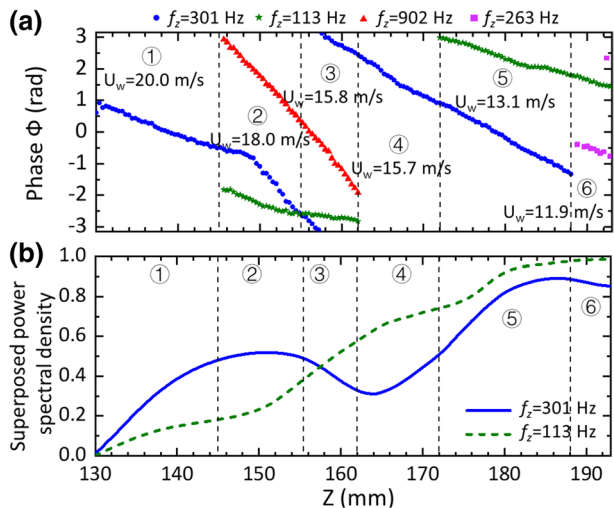
Fig. 17 Distribution of the local frequency response and evolution of the global frequency as a function of downstream distance

frequencies include 113 Hz and 301 Hz. In the third subregion ($Z=153$ mm to 158 mm), the largest frequency response occurs at 113 Hz, and other high-power frequencies include 301 Hz and 902 Hz. The same three dominant frequencies exist in the second and third subregions, although the largest frequency shifts. The fourth subregion ($Z=158$ mm to 172 mm) is analogous to the first regime, and wherein the single, largest frequency response occurs at 301 Hz. In the fifth subregion ($Z=172$ mm to 188 mm), the largest frequency remains 301 Hz, and other high-power frequencies include 113 Hz and 225 Hz. In the last subregion, the largest frequency shifts between the four dominant frequencies (i.e., 113 Hz, 263 Hz, 376 Hz, and 489 Hz (referring to Fig. 15b).

From the above observations, the frequency of 301 Hz dominates in most regions of the flame in the FOV (i.e., occupying 92% of the total height). The second most influential frequency is 113 Hz, dominating a region occupying 52% of the total height. Thus, a natural expectation of the global frequency in the FOV should be 301 Hz. However, the fact is the power density of 113 Hz is markedly larger than that of 301 Hz in the *PSD* plot of global instability shown in Fig. 14. To examine how the local frequencies result in the global instability, the red dashed line shows the evolution of the global frequency as a function of downstream distance. The global frequency along the axial direction shown in Fig. 17 (red dashed line) is calculated by considering a local–global region from Z_0 to Z . As shown, the global frequency keeps at 301 Hz after the first two subregions. It transitions into 113 Hz in the third subregion. Strangely, the global frequency maintains to be 113 Hz after the third subregion, although there still exists the strongest frequency of 301 Hz in the fourth and fifth subregions.

To explain the shift behavior of the global frequency, Fig. 18a shows the phase of local flame edge oscillations along the Z axis. As shown, the phases of oscillations with various frequencies all display continuity at subsequent downstream distances, suggesting the different vortex disturbances moving downstream. The continuous variation of the phase also provides evidence for the soot particles oscillating with the local vortex. As the slope of the phase is indicative of the vortex convective speed along the flame edge, it can be seen that the same vortex-induced disturbance would experience a velocity change when encountering other disturbances. The typical vortex convection speeds in the 6 subregions are

Fig. 18 Panel a: phase of local oscillations along the downstream distances; panel b: superposed power spectral density of the local oscillations of $f_z=113$ Hz and $f_z=301$ Hz along the downstream distances. U_w is the wrinkle convection speed along the flame edge



20 m/s, 18 m/s, 15.8 m/s, 15.7 m/s, 13.1 m/s and 11.9 m/s, respectively. The abrupt change of the phase of 301 Hz mode is due to the occurrence of a new high-frequency disturbance of 902 Hz, which is dominating in subregion 2.

The phase offset of different frequency oscillations varies markedly, resulting in the constructive and destructive interference of these oscillations. It exhibits constructive edge oscillation interference when $\Delta\varphi$ is between 0 and 0.5π radians, and the oscillations neutralize when $\Delta\varphi$ is between 0.5π and 1.5π radians. For example, the maximum phase offset of $f_z=301$ Hz is 2.7π radian throughout the height in Fig. 18a, suggestive of the alternation occurrence of the constructive and destructive interference. For the $f_z=113$ Hz, the phase offset is a range of 0.9π radian, indicative of the major constructive interference. Figure 18b further quantifies the constructive and destructive interferences by showing the superposed power spectral density of these two oscillations (with $f_z=301$ Hz and $f_z=113$ Hz, respectively) along the Z axis. The linear superposition principle is used. As shown, for $f_z=301$ Hz, the superposed *PSD* increases in the first and second subregions. It begins to decrease in the third subregion because the phase offset between this subregion and the first subregion is approaching π rad. A similar decrease in supposed *PSD* due to the π rad phase offset is also observed in the sixth subregion. For $f_z=113$ Hz, the superposed *PSD* keeps increasing as the phase offset is always smaller than π rad. It is close to π rad in the sixth subregion, leading to the weak growth of superposed *PSD* in this subregion. The final result of the superposition shows the stronger *PSD* of $f_z=113$ Hz compared to $f_z=301$ Hz. The result agrees with that shown in Fig. 14b, indicating that the global oscillation of the flame results from the linear superposition of local oscillations at different locations.

5 Summary and Conclusions

Time-resolved 3D measurements of flame edge dynamics were performed on a high-speed jet diffusion flame at 15 kHz. The measurements were performed based on emission tomography implemented with optical endoscopes. Soot radiation and visible chemiluminescence signals are captured to perform the 3D reconstructions of the flame. The 3D reconstructions can resolve the 3D instantaneous flame edge structures with fine-scale corrugations. Instantaneous flame topologies were successfully captured, and highly transient flame dynamics, such as the formation and convection of vortical structures, were also observed by the 3D measurements. The analysis of flame edge deformations shows the vortex-flame interaction dominates the hydrodynamic instability of the flame. Various local frequencies of instability existed along the downstream distance induced by the localized, periodical vortex formations and convections. Those local oscillations exhibited different constructive and destructive interference behaviors. The global oscillation of the flame results from the linear superposition of local oscillations at different locations.

The contributions of the present work are twofold. First, it emphasizes the importance of establishing the relationship between the global and local instabilities, as it is always the case in the practical industry to estimate the global instability of combustor from a localized measurement point/region. The presented method can be readily extended for the conditions where multiple sources of instabilities (i.e., thermo-acoustic instabilities) are involved. Second, the measurement results of the spatially resolved local frequencies distribution along the flow direction are a direct representation of the local vorticity

distribution (Shanbhogue et al. 2009b), but is obtained without introducing further velocity field measurements.

Supplementary Information The online version contains supplementary material available at <https://doi.org/10.1007/s10494-021-00251-4>.

Acknowledgements This study is funded by the National Natural Science Foundation of China under Contractor Nos. 91741108 and 51876179.

Authors' Contribution All authors contributed to the study conception and design. Qingchun Lei, Rongxiao Dong, and Wei Fan contributed to the conception of the study. Rongxiao Dong, Yeqing Chi, Erzhuang Song performed the experiments. The data analysis and manuscript were completed by Rongxiao Dong and Qingchun Lei. All authors commented on previous versions of the manuscript. All authors read and approved the final manuscript.

Funding This study is funded by the National Natural Science Foundation of China under Contractor Nos. 91741108 and 51876179.

Availability of Data and Materials The datasets used or analyzed during the current study are available from the corresponding author on reasonable request.

Compliance with Ethical Standards

Conflict of interest The authors declare that they have no conflict of interest.

References

- Alabdeli, Y., Masri, A., Marquez, G., Starner, S.: Time-varying behaviour of turbulent swirling nonpremixed flames. *Combust. Flame* **146**, 200–214 (2006)
- Allison, P.M., Chen, Y., Ihme, M., Driscoll, J.F.: Coupling of flame geometry and combustion instabilities based on kilohertz formaldehyde PLIF measurements. *Proc. Combust. Inst.* **35**, 3255–3262 (2015)
- Allison, P.M., Frederickson, K., Kirik, J.W., Rockwell, R.D., Lempert, W.R., Sutton, J.A.: Investigation of supersonic combustion dynamics via 50 kHz CH* chemiluminescence imaging. *Proc. Combust. Inst.* **36**, 2849–2856 (2017)
- Anikin, N., Suntz, R., Bockhorn, H.: Tomographic reconstruction of the OH*-chemiluminescence distribution in premixed and diffusion flames. *Appl. Phys. B* **100**, 675–694 (2010)
- Candel, S., Durox, D., Schuller, T., Bourgooin, J.-F., Moeck, J.P.: Dynamics of swirling flames. *Annu. Rev. Fluid Mech.* **46**, 147–173 (2014)
- Cho, K.Y., Satija, A., Pourpoint, T.L., Son, S.F., Lucht, R.P.: High-repetition-rate three-dimensional OH imaging using scanned planar laser-induced fluorescence system for multiphase combustion. *Appl. Opt.* **53**, 316–326 (2014)
- Delichatsios, M.A.: Transition from momentum to buoyancy-controlled turbulent jet diffusion flames and flame height relationships jet diffusion flames and flame height relationships. *Combust. Flame* **92**, 349–364 (1993)
- Doleiden, D., Culler, W., Tyagi, A., Peluso, S., O'Connor, J.: Flame edge dynamics and interaction in a multinozzle can combustor with fuel staging. *J. Eng. Gas. Turbines Power-Trans. ASME* **141** (2019)
- Floyd, J., Lindstedt, P., Kempf, A.: Computed Tomography of Chemiluminescence: A 3D Time Resolved Sensor for Turbulent Combustion. Imperial College, London (2009)
- Floyd, J., Geipel, P., Kempf, A.M.: Computed tomography of chemiluminescence (CTC): instantaneous 3D measurements and phantom studies of a turbulent opposed jet flame. *Combust. Flame* **158**, 376–391 (2011)
- Gatti, M., Gaudron, R., Mirat, C., Zimmer, L., Schuller, T.: Impact of swirl and bluff-body on the transfer function of premixed flames. *Proc. Combust. Inst.* **37**, 5197–5204 (2019)
- Gaudron, R., Gatti, M., Mirat, C., Schuller, T.: Flame describing functions of a confined premixed swirled combustor with upstream and downstream forcing. *J. Eng. Gas. Turbines Power-Trans. ASME* **141** (2019)

- Halls, B.R., Hsu, P.S., Jiang, N., Legge, E.S., Felver, J.J., Slipchenko, M.N., Roy, S., Meyer, T.R., Gord, J.R.: kHz-rate four-dimensional fluorescence tomography using an ultraviolet-tunable narrowband burst-mode optical parametric oscillator. *Optica* **4**, 897–902 (2017)
- Huang, J., Liu, H., Cai, W.: Online in situ prediction of 3-D flame evolution from its history 2-D projections via deep learning. *J. Fluid Mech.* **875**(R2), 1–12 (2019)
- Ishino, Y., Hayashi, N., Bt Abd Razak, I.F., Kato, T., Kurimoto, Y., Saiki, Y.: 3D-CT(Computer Tomography) measurement of an instantaneous density distribution of turbulent flames with a multi-directional quantitative schlieren camera (reconstructions of high-speed premixed burner flames with different flow velocities). *Flow Turbul. Combust.* **96**, 819–835 (2015)
- Kak, A.C., Slaney, M., Wang, G.: Principles of computerized tomographic imaging. *Med. Phys.* **29**, 107 (2002)
- Katta, V.R., Roquemore, W.M., Menon, A., Lee, S.-Y., Santoro, R.J., Litzinger, T.A.: Impact of soot on flame flicker. *Proc. Combust. Inst.* **32**, 1343–1350 (2009)
- Kolhe, P.S., Agrawal, A.K.: Role of buoyancy on instabilities and structure of transitional gas jet diffusion flames. *Flow Turbul. Combust.* **79**, 343–360 (2007)
- Lee, J.G., Santavicca, D.A.: Experimental diagnostics for the study of combustion instabilities in lean premixed combustors. *J. Propul. Power* **19**, 735–750 (2003)
- Lei, Q., Wu, Y., Xiao, H., Ma, L.: Analysis of four-dimensional Mie imaging using fiber-based endoscopes. *Appl. Opt.* **53**, 6389–6398 (2014)
- Li, X., Ma, L.: Capabilities and limitations of 3D flame measurements based on computed tomography of chemiluminescence. *Combust. Flame* **162**, 642–651 (2015)
- Li, T., Pareja, J., Fuest, F., Schütte, M., Zhou, Y., Dreizler, A., Böhm, B.: Tomographic imaging of OH laser-induced fluorescence in laminar and turbulent jet flames. *Meas. Sci. Technol.* **29**, 015206 (2017)
- Liu, B., He, G., Qin, F., Lei, Q., An, J., Huang, Z.: Flame stabilization of supersonic ethylene jet in fuel-rich hot coflow. *Combust. Flame* **204**, 142–151 (2019a)
- Liu, N., Lei, Q., Wu, Y., Ma, L.: 3D tomography reconstruction improved by integrating view registration. *Appl. Opt.* **58**, 2596–2604 (2019b)
- Long, E.J., Hargrave, G.K.: Experimental measurement of local burning velocity within a rotating flow. *Flow Turbul. Combust.* **86**, 455–476 (2011)
- Ma, L., Lei, Q., Wu, Y., Xu, W., Ombrello, T.M., Carter, C.D.: From ignition to stable combustion in a cavity flameholder studied via 3D tomographic chemiluminescence at 20 kHz. *Combust. Flame* **165**, 1–10 (2016)
- Ma, L., Lei, Q., Ikeda, J., Xu, W., Wu, Y., Carter, C.D.: Single-shot 3D flame diagnostic based on volumetric laser induced fluorescence (VLIF). *Proc. Combust. Inst.* **36**, 4575–4583 (2017)
- Mishra, D., Longtin, J.P., Singh, R.P., Prasad, V.: Performance evaluation of iterative tomography algorithms for incomplete projection data. *Appl. Opt.* **43**, 1522–1532 (2004)
- Moeck, J.P., Bourgouin, J.-F., Durox, D., Schuller, T., Candel, S.: Tomographic reconstruction of heat release rate perturbations induced by helical modes in turbulent swirl flames. *Exp. Fluids* **54**, 1498 (2013)
- Mohri, K., Gors, S., Scholer, J., Rittler, A., Dreier, T., Schulz, C., Kempf, A.: Instantaneous 3D imaging of highly turbulent flames using computed tomography of chemiluminescence. *Appl. Opt.* **56**, 7385–7395 (2017)
- Nichols, J.W., Schmid, P.J.: The effect of a lifted flame on the stability of round fuel jets. *J. Fluid Mech.* **609**, 275–284 (2008)
- Nicolas, F., Todoroff, V., Plyer, A., Le Besnerais, G., Donjat, D., Micheli, F., Champagnat, F., Cornic, P., Le Sant, Y.: A direct approach for instantaneous 3D density field reconstruction from background-oriented schlieren (BOS) measurements. *Exp. Fluids* **57** (2015)
- Pareja, J., Johchi, A., Li, T., Dreizler, A., Böhm, B.: A study of the spatial and temporal evolution of auto-ignition kernels using time-resolved tomographic OH-LIF. *Proc. Combust. Inst.* **37**, 1321–1328 (2019)
- Qadri, U.A., Chandler, G.J., Juniper, M.P.: Self-sustained hydrodynamic oscillations in lifted jet diffusion flames: origin and control. *J. Fluid Mech.* **775**, 201–222 (2015)
- Schlumpert, S., Feldhusen, A., Grimm, J.H., Roidl, B., Meinke, M., Schröder, W.: Hydrodynamic instability and shear layer effects in turbulent premixed combustion, *Phys. Fluids* **28** (2016)
- Shanbhogue, S., Shin, D.-H., Hemchandra, S., Plaks, D., Lieuwen, T.: Flame sheet dynamics of bluff-body stabilized flames during longitudinal acoustic forcing. *Proc. Combust. Inst.* **32**, 1787–1794 (2009a)
- Shanbhogue, S.J., Seelhorst, M., Lieuwen, T.: Vortex phase-jitter in acoustically excited bluff body flames. *Int. J. Spray Combust. Dyn.* **1**, 365–388 (2009b)
- Shin, D.-H., Plaks, D.V., Lieuwen, T., Mondragon, U.M., Brown, C.T., McDonnell, V.G.: Dynamics of a longitudinally forced, bluff body stabilized flame. *J. Propul. Power* **27**, 105–116 (2011)

- Steinberg, A.M., Boxx, I., Stöhr, M., Carter, C.D., Meier, W.: Flow–flame interactions causing acoustically coupled heat release fluctuations in a thermo-acoustically unstable gas turbine model combustor. *Combust. Flame* **157**, 2250–2266 (2010)
- Upton, T.D., Verhoeven, D.D., Hudgins, D.E.: High-resolution computed tomography of a turbulent reacting flow. *Exp. Fluids* **50**, 125–134 (2011)
- Weinkauff, J., Greifenstein, M., Dreizler, A., Böhm, B.: Time resolved three-dimensional flamebase imaging of a lifted jet flame by laser scanning. *Meas. Sci. Technol.* **26**, 105201 (2015)
- Wiseman, S.M., Brear, M.J., Gordon, R.L., Marusic, I.: Measurements from flame chemiluminescence tomography of forced laminar premixed propane flames. *Combust. Flame* **183**, 1–14 (2017)
- Worth, N.A., Dawson, J.R.: Tomographic reconstruction of OH* chemiluminescence in two interacting turbulent flames. *Meas. Sci. Technol.* **24**, 024013 (2012)
- Xia, Y., Lei, Q., Chi, Y., Fan, W., Tao, B.: An improved camera calibration method for 3D flame measurements based on tomographic reconstruction, ASPACC 2019. Fukuoka, Japan (2019)
- Zhang, H., Mastorakos, E.: Prediction of global extinction conditions and dynamics in swirling non-premixed flames using LES/CMC modelling. *Flow Turbul. Combust.* **96**, 863–889 (2015)